NIH Public Access
Author Manuscript
IEEE Trans Med Imaging. Author manuscript; available in PMC 2010 July 13.

Published in final edited form as:
IEEE Trans Med Imaging. 2008 ; 27(7): 925–933. doi:10.1109/TMI.2008.923950.

Planogram Rebinning With the Frequency-Distance Relationship

Kyle Champley,
Department of Radiology, University of Washington, Seattle, WA 98195 USA

Michel Defrise [Member, IEEE],
Division of Nuclear Medicine, Vrije Universiteit Brussel, B-1090, Belgium

Rolf Clackdoyle [Member, IEEE],
CNRS Laboratoire Hubert Curien, Universite Jean Monnet, 42000 St. Etienne, France

Raymond R. Raylman [Member, IEEE], and
Department of Radiology, West Virginia University, Morgantown WV 26506

Paul E. Kinahan [Senior Member, IEEE]
Department of Radiology, University of Washington, Seattle, WA 98195 USA

Kyle Champley: champlk@u.washington.edu; Michel Defrise: mdefrise@ulb.ac.be; Rolf Clackdoyle: rolf.clackdoyle@univ-st-etienne.fr; Raymond R. Raylman: rraylman@hsc.wvu.edu; Paul E. Kinahan: kinahan@u.washington.edu

Abstract

We present an efficient rebinning algorithm for positron emission tomography (PET) systems with panel detectors. The rebinning algorithm is derived in the planogram coordinate system which is the native data format for PET systems with panel detectors and is the 3-D extension of the 2-D linogram transform developed by Edholm. Theoretical error bounds and numerical results are included.

Index Terms

Image reconstruction; medical imaging; positron emission tomography; X-ray transform

I. Introduction

We present a new rebinning algorithm for positron emission tomography (PET) systems with parallel planar detectors. This work is motivated by a new positron emission mammography/PET PEM-PET system developed at West Virginia University [1]. The scanner is comprised of four planar detectors that form a box, with coincidences acquired between opposite detector heads. The detector heads are capable of rotation in step-and-shoot mode to acquire full tomographic data. The distance between detector panels is 26.4 cm. Each detector head is 206 mm wide by 151 mm high and composed of 94 × 70 LYSO crystals. The LYSO crystals are 2 mm × 2 mm wide and 15 mm thick with a separation of 0.1 mm between the crystals. The system also incorporates a method for biopsy guidance. Compression plates are used to stabilize the breast.

Fast reconstruction algorithms are required by this system for a few reasons. One motivation for high quality, rapid image reconstruction is the detection of small lesions (less than 5 mm), so that if a lesion is detected an image-guided biopsy can be performed while the patient remains on the imaging table. Since both breasts are scanned with a possible biopsy

Correspondence to: Kyle Champley, champlk@u.washington.edu.

NIH-PA Author Manuscript
NIH-PA Author Manuscript
NIH-PA Author Manuscript

NIH-PA Author Manuscript

NIH-PA Author Manuscript

NIH-PA Author Manuscript

performed on either, the need for rapid image reconstruction is compounded. We also wish to perform dynamic studies. In this case, many images must be reconstructed. This would be a significant burden with fully 3-D image reconstruction algorithms and thus we set out to develop an efficient rebinning algorithm.

The rebinning algorithm that we develop below determines (through observing relationships in Fourier space) how to best reassign the oblique data to the direct data. After the rebinning algorithm is applied, one can use any 2-D reconstruction algorithm (e.g., filtered backprojection or OSEM) on the stack of linograms. We name our rebinning algorithm the planogram frequency-distance rebinning algorithm (PFDR). The PFDR algorithm is derived in the planogram coordinate system [2] which is the native data format for PET systems with panel detectors and is the 3-D extension of the 2-D linogram transform developed by Edholm [3].

An exact rebinning algorithm for PET systems with panel detectors has been developed by Kao *et al.* [4]. It is similar to the rebinning algorithm that we develop here, but a detailed comparison of the two methods is beyond the scope of this paper. The Kao rebinning algorithm is an exact rebinning algorithm based on John's Equation [5] which requires finite difference methods to approximate derivatives in the data. Data derivatives are known to often increase noise as observed with the exact rebinning algorithm based on John's equation for cylindrical scanners [6]. This noise amplification was noted by Kao as a problem in their algorithm. In contrast, the PFDR algorithm is an approximate rebinning algorithm that is more computationally efficient and involves numerically stable operations. In addition, we derive theoretical error bounds in Theorem IV.4 that characterize the distribution of the errors introduced by the PFDR algorithm. To the best of our knowledge, this is the first time that such as error bound has been obtained for a rebinning algorithm in PET. We test the PFDR algorithm with numerical experiments from both simulated and measured data from our PEM-PET system. Noise and contrast metrics of images produced with the PFDR algorithm are computed.

Other than rebinning algorithms, there are a few other reconstruction methods for PET systems with planar detectors. Two alternatives to rebinning algorithms are the fully 3-D OSEM algorithm [7] and the direct planogram method (a fully 3-D analytic reconstruction method) developed by Brasse *et al.* [2].

II. Planogram Geometry and Transform

Consider two planar detectors given by

$$\{(x, y, z): -L \le x \le L, y=R, -H \le z \le H\}$$
$$\{(x, y, z): -L \le x \le L, y=-R, -H \le z \le H\}.$$

We will parameterize each line of response (LOR) by $(u_0, v_0, u_1, v_1) \in \mathbb{R}^4$, where (u_0, u_1) are the x- and z-co-ordinates, respectively, of the intersection of the LOR with the plane $y = 0$, v_0 is the y–x slope of the LOR, and v_1 is the y–z slope of the LOR. Thus, the LORs of planogram data are given by

$$\{(x, y, z): x=u_0 - v_0 y, y \in \mathbb{R}, z=u_1 - v_1 y\}$$

and the planogram transform is given by

NIH-PA Author Manuscript

NIH-PA Author Manuscript

NIH-PA Author Manuscript

$$g(u_0, v_0, u_1, v_1) \equiv \int_{\mathbb{R}} f(u_0 - v_0 y, y, u_1 - v_1 y) dy$$

for $(u_0, v_0, u_1, v_1) \in \mathbb{R}^4$. The function $f: \mathbb{R}^3 \to \mathbb{R}$ quantifies that distribution of the radiotracer and $g: \mathbb{R}^4 \to \mathbb{R}$ models the PET coincidence data. Note that the planogram transform weighs the raw data by $1/\sqrt{1+v_0^2+v_1^2}$. See Fig. 1 for a sketch of the detector orientation and the parameterization of the LORs. The variables (v_0, v_1) are playing the role of the angular orientation of the LOR, so $g(\cdot, v_0, \cdot, v_1)$ is a 2-D parallel beam projection. Planogram coordinates can be expressed as linear transformations of the local detector coordinates by

$$\begin{aligned} u_0 &= \tfrac{1}{2}(s_A - s_B), & v_0 &= \tfrac{1}{2R}(s_A + s_B) \\ u_1 &= \tfrac{1}{2}(t_A + t_B), & v_1 &= \tfrac{1}{2R}(t_A - t_B). \end{aligned}$$

(see Fig. 1).

The term planogram comes from the fact that the collection of lines intersecting a fixed point lies on a 2-D plane in the 4-D data space. The planogram transform is the 3-D extension of the linogram transform, which is given by

$$g(u_0, v_0) = \int_{\mathbb{R}} f(u_0 - v_0 y, y) dy.$$

The linogram transform was first introduced by Edholm [3].

In the following, we will refer to the *direct* data as the data where $v_1 = 0$ and the *oblique* data as the data where $v_1 \neq 0$. Note that when $v_1 = 0$, the planogram transform reduces to a stack of linogram transforms (one for each u_1). We will refer to the support of a function, $h: \mathbb{R}^n \to \mathbb{R}$, as the set

$$\operatorname{supp}(h) \equiv \overline{\{x \in \mathbb{R}^n : h(x) \neq 0\}}$$

where the overline denotes the closure of the set. The indicator function of a set **A** will be denoted by

$$\mathbf{1}_{\mathbf{A}}(x) = \begin{cases} 1, & x \in \mathbf{A} \\ 0, & x \notin \mathbf{A} \end{cases}.$$

Binary subscripts mark which variables for which we have taken the Fourier transform. For example, if $h \in L^1(\mathbb{R}^2)$, then the Fourier transform of h in the second variable is

$$\widehat{h}_{01}(x, Y) = \int_{\mathbb{R}} h(x, y) e^{-2\pi i y Y} dy.$$

NIH-PA Author Manuscript

NIH-PA Author Manuscript

NIH-PA Author Manuscript

III. Domain and Support of the Planogram Transform

Since the planar detectors are of finite size, we cannot measure the planogram transform for all values of $(u_0, v_0, u_1, v_1) \in \mathbb{R}^4$. The measured domain is the direct product of two diamond-shaped regions given by

$$\begin{aligned}\mathbf{M}_m &= \mathbf{M}_{mL} \times \mathbf{M}_{mH} \\ &\equiv \left\{(u_0, v_0): |u_0| \le L, |v_0| \le \tfrac{1}{R}(L - |u_0|)\right\} \times \left\{(u_1, v_1): |u_1| \le H, |v_1| \le \tfrac{1}{R}(H - |u_1|)\right\}.\end{aligned}$$

Now suppose that

$$\operatorname{supp}(f) \subseteq \mathbf{S}_f \equiv \{(x, y, z): x^2 + y^2 < a^2, z \in (-c, c)\}$$

where $a < \min(L, R)$ and $c < H$, i.e., $\operatorname{supp}(f)$ is contained in a cylinder entirely within the field of view of the PET system. The support of the planogram transform is contained in the direct product of two butterfly-shaped regions given by

$$\begin{aligned}\operatorname{supp}(g) \subseteq \mathbf{S}_g \equiv &\left[\{(u_0, v_0): |u_0| \le a, v_0 \in \mathbb{R}\} \cup \left\{(u_0, v_0): |u_0| > a, |v_0| \ge \frac{1}{a}\sqrt{u_0^2 - a^2}\right\}\right] \\ &\times \left[\{(u_1, v_1): |u_1| \le c, v_1 \in \mathbb{R}\} \cup \left\{(u_1, v_1): |u_1| > c, |v_1| \ge \frac{|u_1| - c}{a}\right\}\right].\end{aligned}$$

See Fig. 2 for a sketch of the sets $\mathbf{S}_g$ and $\mathbf{M}_m$. After observing the intersection of $\mathbf{M}_m$ and $\mathbf{S}_g$, we see that there is no truncation of the projection (i.e., no truncation for the variables (u_0, u_1)) for

$$\begin{aligned}|v_0| &\le v_{m0} \equiv \tfrac{RL - a\sqrt{R^2 + L^2 - a^2}}{R^2 - a^2} \\ |v_1| &\le v_{m1} \equiv \tfrac{H - c}{R + a}.\end{aligned}$$

In other words, for $|v_0| > v_{m0}$ or $|v_1| > v_{m1}$ there exists LORs that intersect the support of f that are not measured by the PET system due to the finite size of the detectors. All of the LORs corresponding to $|v_0| \le v_{m0}$ and $|v_1| \le v_{m1}$ have either been measured or do not intersect the support of f and thus $g = 0$ for these LORs.

Now define

$$\mathbf{M}_{m0} \equiv \{(u_0, v_0, u_1, v_1) \in \mathbf{M}_m: |v_0| \le v_{m0}\}$$

and the measured planogram by

$$g^m(u_0, v_0, u_1, v_1) \equiv \begin{cases} g(u_0, v_0, u_1, v_1), & (u_0, v_0, u_1, v_1) \in \mathbf{M}_m \\ 0, & (u_0, v_0, u_1, v_1) \notin \mathbf{M}_m \end{cases}$$

NIH-PA Author Manuscript

NIH-PA Author Manuscript

NIH-PA Author Manuscript

and the restricted planogram by

$$g^{m0}(u_0, v_0, u_1, v_1) \equiv \begin{cases} g(u_0, v_0, u_1, v_1), & (u_0, v_0, u_1, v_1) \in \mathbf{M}_{m0}, \\ 0, & (u_0, v_0, u_1, v_1) \notin \mathbf{M}_{m0}. \end{cases}$$

We will refer to $g(u_0, v_0, u_1, v_1)$, where $(u_0, v_0, u_1, v_1) \in \mathbb{R}^4$ as the ideal data.

The restricted data is defined so that the 1-D projections (1-D projection defined by $g^{m0}(\cdot, v_0, u_1, v_1)$) are not truncated. This will provide an easier analysis in the development of our rebinning algorithm. The restriction of $|v_1| \leq v_{m1}$ is necessary for fully 3-D analytic reconstruction algorithms [2], but is not necessary for rebinning algorithms and thus is not mentioned in the remainder of our discussion.

IV. Rebinning Algorithms

A. Development

The acquired planogram data is a 4-D data set used to determine a 3-D object, thus there is redundancy in the measurements (in the noise-free case). One could reconstruct the image only using the direct data, ignoring the redundant, oblique data. However, one can improve the signal-to-noise ratio of the data with the use of a rebinning algorithm. Compared to fully 3-D reconstruction algorithms, most rebinning algorithms speed up the reconstruction at the cost of reduced accuracy. One rebinning technique is known as single slice rebinning (SSRB) [8]. In the planogram coordinate system, the SSRB algorithm is given by

$$g^{\mathrm{SSRB}}(u_0, v_0, z) \equiv \frac{1}{N(z)} \int_{-v_{1\max}}^{v_{1\max}} g(u_0, v_0, z, v_1) \mathbf{1}_{\mathbf{M}_{mH}}(z, v_1) dv_1$$
$$N(z) \equiv \int_{-v_{1\max}}^{v_{1\max}} \mathbf{1}_{\mathbf{M}_{mH}}(z, v_1) dv_1$$

where the rebinned data g^{SSRB} is a stack of linograms in our case.

The rebinning algorithm that we develop below determines (through observing relationships in Fourier space) how to best reassign the oblique data to the direct data. After the rebinning algorithm is applied, one can use any 2-D reconstruction algorithm (e.g., filtered backprojection or OSEM) on the stack of linograms.

We now develop the rebinning formula that can be applied to the ideal, measured, or restricted planogram data. In the case of ideal data, the rebinning formula is exact, otherwise the rebinning formula is approximate and in this case we develop theoretical error bounds. Below is a sequence of theorems that will establish these results (some proofs are in the Appendix). Our rebinning algorithm is a direct result of Theorem IV.2, but since the Proof of Theorem IV.2 relies on Theorem IV.1, we start with the restricted planogram. We will return to Theorem IV.1 when developing our theoretical error bounds.

Theorem IV.1—Let $f \in L^2(\mathbb{R}^3)$, $\mathrm{supp}(f) \subseteq \mathbf{S}_f$, and let g^{m0} be the restricted planogram as defined above. Then for $(u_1, v_1) \in \mathbf{M}_{mH}$

$$\widehat{g}^{m0}_{1100}(U_0, V_0, u_1, v_1) = \frac{1}{|U_0|} \int_{\mathbb{R}} \int_{\mathbb{R}} \widehat{f}_{111}(U_0, Y, Z) \quad (1)$$

NIH-PA Author Manuscript

NIH-PA Author Manuscript

NIH-PA Author Manuscript

$$\times e^{2\pi i[-\frac{V_0}{U_0}Y+(u_1+v_1\frac{V_0}{U_0})Z]} \times \mathbf{1}_{\{(U_0,Y,Z):|Y-v_1Z|\le v_{m0}|U_0|\}}(U_0,Y,Z)\,dY\,dZ \quad (2)$$

$$=\widehat{f}_{100}(U_0,y,u_1-v_1y) * \frac{\sin(2\pi v_{m0}U_0y)}{\pi U_0y}\Big|_{y=-V_0/U_0} \quad (3)$$

where the indicator function

$$\mathbf{1}_{\{(U_0,Y,Z):|Y-v_1Z|\le v_{m0}|U_0|\}}(U_0,Y,Z)$$

is plotted for $v_1 = 0$ and $v_1 \neq 0$ in Fig. 3.

The Proof of Theorem IV.1 is in the Appendix.

Theorem IV.2—Let $f \in L^2(\mathbb{R}^3)$, $\mathrm{supp}(f) \subseteq \mathbf{S}_f$. Then we have that

$$\widehat{g}_{1100}(U_0,V_0,u_1,v_1)=\frac{1}{|U_0|}\widehat{f}_{100}\left(U_0,-\frac{V_0}{U_0},u_1+v_1\frac{V_0}{U_0}\right).$$

Proof: From Theorem IV.1 we have that

$$\begin{aligned}&\widehat{g}_{1100}(U_0,V_0,u_1,v_1)\\ &=\lim_{v_{m0}\to\infty}\widehat{g}^{m0}_{1100}(U_0,V_0,u_1,v_1)\\ &=\lim_{v_{m0}\to\infty}\widehat{f}_{100}(U_0,y,u_1-v_1y) * \frac{\sin(2\pi v_{m0}U_0y)}{\pi U_0y}\Big|_{y=-V_0/U_0}\\ &=\frac{1}{|U_0|}\widehat{f}_{100}\left(U_0,-\frac{V_0}{U_0},u_1+v_1\frac{V_0}{U_0}\right).\end{aligned} \quad (4)$$

From Theorem IV.2 we have that

$$\widehat{g}_{1100}(U_0,V_0,u_1,0)=\frac{1}{|U_0|}\widehat{f}_{100}\left(U_0,-\frac{V_0}{U_0},u_1\right) \quad (5)$$

$$=\widehat{g}_{1100}\left(U_0,V_0,u_1-v_1\frac{V_0}{U_0},v_1\right). \quad (6)$$

Equation (6) is the key to the PFDR algorithm. We can use (6) to rebin the 4-D planogram into a stack of linograms by

$$g^{\mathrm{PFDR}}_{110}(U_0,V_0,z) \equiv \frac{1}{N(-V_0/U_0,z)} \quad (7)$$

NIH-PA Author Manuscript

NIH-PA Author Manuscript

NIH-PA Author Manuscript

$$\times \int_{-v_{1\max}}^{v_{1\max}} \widehat{g}_{1100}(U_0, V_0, z-(V_0/U_0)v_1, v_1) \times \mathbf{1}_{\mathbf{M}_{mH}}(z-(V_0/U_0)v_1, v_1)dv_1 \quad (8)$$

$$N(-V_0/U_0, z) \equiv \int_{-v_{1\max}}^{v_{1\max}} \mathbf{1}_{\mathbf{M}_{mH}}(z-(V_0/U_0)v_1, v_1)dv_1. \quad (9)$$

The term $v_{1\max}$ is an arbitrary limit placed on the maximum oblique angle for which we wish to perform the rebinning. This quantity may be limited to avoid excessive parallax errors or limited simply due to the detector geometry.

The rebinning algorithm can be performed in three steps. First we take the Fourier transform of $g(u_0, v_0, u_1, v_1)$ in the first two variables for each $(u_1, v_1) \in \mathbf{M}_{mH}$. Now let $N(-V_0/U_0, z)$ be the number of values of $\hat{g}_{1100}(U_0, V_0, z - v_1 V_0/U_0, v_1)$ that we have computed (for varying v_1) for each fixed set of values $(-V_0/U_0, z)$. Then we compute the normalized sum over v_1 by

$$\widehat{g}_{110}^{\mathrm{PFDR}}(U_0, V_0, z) = \frac{1}{N(-V_0/U_0, z)} \times \sum_{v_1}^{N(-V_0/U_0, z)} \widehat{g}_{1100}\left(U_0, V_0, z - v_1 \frac{V_0}{U_0}, v_1\right)$$

which is the analog of (8) when v_1 is discrete. Finally, we compute an inverse Fourier transform of $\widehat{g}_{110}^{\mathrm{PFDR}}(U_0, V_0, z)$ in the first two variables for each z. This is our rebinned data. Then we can reconstruct this rebinned data with any 2-D reconstruction algorithm for each axial slice.

We would like to apply this rebinning formula to the measured or restricted planogram and from (4) we see that this could very well be possible for the restricted planogram. From Theorem IV.1 we have

$$\widehat{g}_{1100}^{m0}(U_0, V_0, u_1, v_1) = \frac{1}{|U_0|}\widehat{f}_{100}^{*}\left(U_0, -\frac{V_0}{U_0}, u_1 + v_1\frac{V_0}{U_0}\right) \approx \frac{1}{|U_0|}\widehat{f}_{100}\left(U_0, -\frac{V_0}{U_0}, u_1 + v_1\frac{V_0}{U_0}\right)$$

where f^* is the result of filtering f by

$$\mathbf{1}_{\{(U_0,Y,Z):|Y-v_1Z|\le v_{m0}|Z|\}}(U_0, Y, Z).$$

Note that this approximation becomes increasingly accurate as $v_{m0} \to \infty$ or $U_0 \to \infty$.

The relations (3, 4, 6) were first shown by Defrise *et al.* in an unpublished note [9]. Also note that from (4) with $y = -V_0/U_0$ we have that

$$\widehat{g}_{1100}(U_0, -yU_0, u_1, v_1) = \frac{1}{|U_0|}\widehat{f}_{100}(U_0, y, u_1 - v_1 y). \quad (10)$$

This relationship is known as the frequency-distance relationship. It says that for a fixed (u_1, v_1) a line through the center of the 2-D transform of the data with slope $-y$ is related to the

NIH-PA Author Manuscript

NIH-PA Author Manuscript

NIH-PA Author Manuscript

image f at a distance y from the center of the of coincidence detector panels. The rebinning formula that we described above is a direct consequence of this relation and thus we appropriately name our rebinning algorithm the planogram freqency-distance rebinning (PFDR) algorithm.

We note that the frequency distance relationship is an exact relationship only in the planogram/linogram coordinate system. For sinograms this is an approximate relationship.

Thus far we have provided an argument for the use of the PFDR rebinning algorithm to restricted and ideal data. We wish to apply this rebinning algorithm to the practical case of measured data. We start with the following theorem.

Theorem IV.3—Let $f \in L^2(\mathbb{R}^3)$, $\text{supp}(f) \subseteq \mathbf{S}_f$, and let g^m be the measured planogram as defined above. Then for $(u_1, v_1) \in \mathbf{M}_{mH}$

$$\widehat{g}^m_{1100}(U_0, V_0, u_1, v_1) = \int_{\mathbb{R}} \int_{\mathbb{R}} \widehat{f}_{100}(X, t, u_1 - v_1 t) \times \frac{\cos(2\pi L(U_0 - X)) - \cos(2\pi \frac{L}{R}(V_0 + tX))}{\pi^2(\frac{1}{R}(V_0 + tX)^2 - R(U_0 - X)^2)} dt\, dX$$

$$\begin{aligned}
\widehat{g}^m_{1100}(U_0, -yU_0, z + yv_1, v_1) = \frac{1}{|U_0|} \int_{\mathbb{R}^2} dY\, dZ\, \widehat{f}_{111}(U_0, \\
Y, Z) \times \mathbf{1}_{\{(U_0, Y, Z): |Y - v_1 Z| \le (L/R)|U_0|\}}(U_0, \\
Y, Z) e^{2\pi i [yY + zZ]} \\
- \int_{\mathbb{R}^3} \frac{1}{|X|} \widehat{f}_{111}(X, \\
Y, Z) e^{2\pi i [y(\frac{U_0}{X}(Y - v_1 Z) + v_1 Z) + zZ]} \times \mathbf{1}_{\{(X, Y, Z): |v_{m0}|X| < |Y - v_1 Z| \le (L/R)|X|\}}(X, \\
Y, Z) \times \left(\frac{\sin\left(2\pi a \frac{(U_0 - X)}{|X|} \sqrt{X^2 + (Y - v_1 Z)^2}\right)}{\pi(U_0 - X)} - \frac{\sin\left(2\pi \frac{(U_0 - X)}{|X|}(L|X| - R|Y - v_1 Z|)\right)}{\pi(U_0 - X)} \right) dX\, dY\, dZ.
\end{aligned}$$

We omit the Proof of Theorem IV.3 because it simply follows from the same argument as the Proof of Theorem IV.1. Note the similarity between the relationship given above and the relationship between the restricted data and the image, given by

$$g^{m0}_{1100}(U_0, -yU_0, z + yv_1, v_1) = \frac{1}{|U_0|} \int_{\mathbb{R}^2} dY\, dZ\, \widehat{f}_{111}(U_0, Y, Z) \times \mathbf{1}_{\{(U_0, Y, Z): |Y - v_1 Z| \le v_{m0}|U_0|\}}(U_0, Y, Z) \times e^{2\pi i [yY + zZ]}.$$

Using the same argument as we did above for the restricted data, one can see that

$$\widehat{g}^m_{1100}(U_0, V_0, u_1, 0) \approx \widehat{g}^m_{1100}\left(U_0, V_0, u_1 - v_1 \frac{V_0}{U_0}, v_1\right)$$

and thus it is reasonable to use the PFDR algorithm with the measured data also.

NIH-PA Author Manuscript

NIH-PA Author Manuscript

NIH-PA Author Manuscript

B. Error Bounds

The next theorem establishes error bounds for the SSRB and PFDR rebinning algorithms when applied to the restricted data.

Theorem IV.4—Let $\Omega = [-W, W]^2 \subseteq \mathbb{R}^2$ and $f \in L^2(\mathbb{R}^2)$ be such that $\text{supp}(f) \subseteq \mathbf{S}_f$ and for any $U_0 \in \mathbb{R}$

$$\int\int_{\Omega^c} |\widehat{f}_{111}(U_0, Y, Z)| dY\, dZ < \varepsilon$$

for some small $\varepsilon > 0$. Then the PFDR error can be characterized by

$$|\widehat{g}^{m0}_{1100}(U_0, -yU_0, z+v_1 y, v_1) - \widehat{g}^{m0}_{1100}(U_0, -yU_0, z, 0)| \leq \frac{1}{|U_0|}\left[\varepsilon + \left\|\widehat{f}_{111}(U_0, \cdot, \cdot)\right\|_{L^2(\mathbb{R}^2)} \times \left(\int_{-W}^{W}\int_{-W}^{W} |\mathbf{1}_{\mathbf{E}_0}(Y,Z) - \mathbf{1}_{\mathbf{E}_{v_1}}(Y,Z)| dY\, dZ\right)^{1/2}\right]$$

and the SSRB error can be characterized by

$$|\widehat{g}^{m0}_{1100}(U_0, -yU_0, z, v_1) - \widehat{g}^{m0}_{1100}(U_0, -yU_0, z, 0)| \leq \frac{1}{|U_0|}\left[\varepsilon + \left\|\widehat{f}_{111}(U_0, \cdot, \cdot)\right\|_{L^2(\mathbb{R}^2)} \times \left(\int_{-W}^{W}\int_{-W}^{W} |\mathbf{1}_{\mathbf{E}_0}(Y,Z) - \mathbf{1}_{\mathbf{E}_{v_1}}(Y,Z) e^{-2\pi i v_1 y Z}|^2 dY\, dZ\right)^{1/2}\right]$$

where

$$\mathbf{E}_0 = \{(Y,Z) \in \mathbb{R}^2 : |Y| \leq v_{m0}|U_0|\}$$
$$\mathbf{E}_{v_1} = \{(Y,Z) \in \mathbb{R}^2 : |Y - v_1 Z| \leq v_{m0}|U_0|\}.$$

The Proof of Theorem IV.4 follows from Theorem IV.1 and the Cauchy-Schwarz inequality.

Note that $|\mathbf{1}_{\mathbf{E}_0}(Y,Z) - \mathbf{1}_{\mathbf{E}_{v1}}(Y,Z)| = \mathbf{1}_{\mathbf{E}_0 \Delta \mathbf{E}_{v1}}(Y, Z)$, where

$$\mathbf{E}_0 \Delta \mathbf{E}_{v_1} = \{(Y,Z) \in \mathbf{E}_0 \cup \mathbf{E}_{v_1} : (Y,Z) \notin \mathbf{E}_0 \cap \mathbf{E}_{v_1}\}.$$

Also note that for $x, y \in \mathbb{C}$, $||x| - |y|| \leq |x - y|$, so

$$|\mathbf{1}_{\mathbf{E}_0}(Y,Z) - \mathbf{1}_{\mathbf{E}_{v_1}}(Y,Z)| = \left|\left|\mathbf{1}_{\mathbf{E}_0}(Y,Z)| - |\mathbf{1}_{\mathbf{E}_{v_1}}(Y,Z)\right|\right| = \left|\left|\mathbf{1}_{\mathbf{E}_0}(Y,Z)| - |\mathbf{1}_{\mathbf{E}_{v_1}}(Y,Z) e^{-2\pi i v_1 y Z}\right|\right| \leq |\mathbf{1}_{\mathbf{E}_0}(Y,Z) - \mathbf{1}_{\mathbf{E}_{v_1}}(Y,Z) e^{-2\pi i v_1 y Z}|$$

and thus

$$|\mathbf{1}_{\mathbf{E}_0}(Y,Z) - \mathbf{1}_{\mathbf{E}_{v_1}}(Y,Z)| = |\mathbf{1}_{\mathbf{E}_0}(Y,Z) - \mathbf{1}_{\mathbf{E}_{v_1}}(Y,Z)|^2 \leq |\mathbf{1}_{\mathbf{E}_0}(Y,Z) - \mathbf{1}_{\mathbf{E}_{v_1}}(Y,Z) e^{-2\pi i v_1 y Z}|^2.$$

NIH-PA Author Manuscript

NIH-PA Author Manuscript

NIH-PA Author Manuscript

Although the above does not prove than the PFDR error is less that the error for SSRB, it does indicate that this is most likely the case. The above error bound also shows how the accuracy of images reconstructed by application the SSRB algorithm depend on y, the distance from the center of the field of view of the system, while the accuracy of images reconstructed by application of the PFDR algorithm does not depend on this parameter. We note that the variable y is indeed the distance from the center of the field of view as was shown in Theorem IV.1.

Unfortunately, one does not have such a nice representation of the error with measured data as we have with the restricted data. The above also establishes that the PFDR algorithm is essentially exact for $W \leq (v_{m0}|U_0|)/(|v_1| + 1)$ or $v_1 = 0$ because

$$\int_{-W}^{W}\int_{-W}^{W} \mathbf{1}_{\mathbf{E}_0 \Delta \mathbf{E}_{v_1}} \, dY \, dZ = 0 \quad (11)$$

in this region.

In practice W is the Nyquist rate determined by the geometry of the system and thus is fixed. But in such a situation, we reconstruct a bandlimited function, bandlimited with this rate. Thus it is reasonable to assume that ε is extremely small if not equal to zero.

V. Numerical Results

In this section, we describe the numerical experiments for which we tested the PFDR rebinning algorithm. We used both simulated data (analytic simulation implemented by ray tracing) and data from our PEM-PET system whose specifications were described in the introduction of this paper. In either case, the same software was used to reconstruct our image. Detector response, attenuation, etc. were not incorporated in our simulation.

Three gantry positions were used (0°, 30°, 60°) to acquire full tomographic data for a field-of-view of size 12×12×15.1 cm. Since our PEM-PET system has two sets of detectors in coincidence, three gantry positions result in six sets of data. We have implemented three different reconstruction algorithms for the purpose of comparison. The PFDR and SSRB rebinning algorithms are implemented with a maximum copolar acceptance angle of 15°, i.e., $v_{1\max} = \tan(15°)$. Depending on the axial slice, this entails the rebinning of up to 67 oblique planes to one direct plane. To illustrate the noise-reducing capabilities of the PFDR and SSRB rebinning algorithms we also reconstructed images using only the direct data, i.e., the data where $v_1 = 0$. After reducing our 4-D set of data (g^m) into a 3-D set of data, all three methods (PFDR, SSRB, and direct) use the same 2-D linogram filtered backprojection [10] software applied to each axial slice of the data to reconstruct the image. All reconstructed images displayed in this paper are comprised of a volume of 230×230×276 cubic voxels with side length $d/4$ cm = 0.0525 cm, where $d = 0.21$ cm is the detector pixel sampling distance. The units of the axes of the reconstructed images is measured in centimeters.

To illustrate that the PFDR algorithm reduces noise while introducing few distortions, we tested the algorithm with noisy simulated data from a four-quadrant hot sphere phantom. This phantom is composed of a warm background with wedge-shaped regions of hot spheres (contrast between hot spheres and background is 5:1) of diameters equal to 0.32, 0.24, 0.16, and 0.12 cm. Noisy data was produced by Poisson noise generation software applied to the values obtained by the analytic line tracing calculations. A total of 1163×10^6 events were simulated. The PFDR and SSRB algorithms use approximately 559×10^6 of these events and the Direct reconstruction uses approximately 24×10^6 of these events. Reconstruction images are shown in Figs. 4 and 5.

NIH-PA Author Manuscript

NIH-PA Author Manuscript

NIH-PA Author Manuscript

The images reconstructed from the four-quadrant hot sphere phantom were evaluated by measuring the contrast recovery coefficients and noise, see Fig. 6. The contrast recovery coefficients were calculated for each of the diameters of the hot spheres. Noise was calculated with reconstructions from twenty five independent realizations of the data.

As shown by Theorem IV.4, the accuracy of the SSRB algorithm degrades with increasing distance from the center of the scanner while the accuracy of the PFDR algorithm does not depend on this parameter. To support this claim, we simulated a phantom of 13 rod sources stacked on top of each other in the axial direction. Each rod has a rectangular cross section and is 5×0.42×0.42 cm in size. A gap of size 0.42 cm is placed between each rod. The results of reconstructing this phantom with the PFDR and SSRB rebinning algorithms with $v_{1\max} = \tan(15°)$can be found in Fig. 7.

The PFDR and SSRB algorithms were also tested with measured data from our PEM-PET system using a micro-Derenzo phantom (Fig. 8) and a phantom consisting of two trans-axial line sources (Fig. 9). Scatter and attenuation correction algorithms were not implemented. The micro-Derenzo phantom is comprised of vertically oriented cylinders of diameters equal to 0.48, 0.40, 0.32, 0.24, 0.16, and 0.12 cm. A maximum polar acceptance angle of $v_{1\max} = \tan(15°)$ was used in the reconstructions of both phantoms. The choice of $v_{1\max}$ is due to parallax considerations.

The reconstruction software was written in C++ and experiments were ran on a 2.3-GHz PowerPC G5 processor. Images of voxel side length 0.21/2 cm (image is 115×115×138 voxels), 0.21/3 cm (image is 172×172×207 voxels), and 0.21/4 cm (image is 230×230×276 voxels) were reconstructed with the Direct, SSRB, and PFDR algorithms and their computation times are given in Table I.

VI. Discussion and Conclusion

We have developed a rebinning algorithm that is extremely efficient and easy to implement as it only requires FFT operations and a simple summation to reorganize the data into a 3-D set. Initial numerical results show that the PFDR algorithm significantly reduces noise while providing good resolution in the axial direction compared to a reconstruction that would only incorporate the direct data. The quality of the axial resolution indicates that the approximation made by the PFDR algorithm is acceptable for PET systems with panel detectors.

Theorem IV.4 provides slice-by-slice error bounds for the PFDR and SSRB rebinning algorithms. Not only do we see that the PFDR is more accurate, but we also see how the accuracy of SSRB degrades as we move away from the center of the field of view. The images in Figs. 7 and 9 support the conclusion of this theorem. Notice how the resolution of images reconstructed with the SSRB algorithm degrade with increasing distance from the center of the scanner while the resolution of the images reconstructed with the PFDR remains constant.

The rebinning algorithm that we have developed here is similar to the Fourier rebinning (FORE) algorithm, a rebinning algorithm developed by Defrise *et al.* [11] for PET systems with detectors oriented on a cylinder. Our algorithm is similar in the fact that one finds the relation between the direct and oblique data in Fourier space. The original motivation for this work was to derive similar relationships derived in [11] for the planogram geometry. The relationships between the direct and oblique Radon data in Fourier space can also be derived by John's equation [5].

NIH-PA Author Manuscript

NIH-PA Author Manuscript

NIH-PA Author Manuscript

One could take the planogram data from all gantry rotations and interpolate the data into the sinogram data format by placing a virtual cylinder inside the PEM-PET gantry. This however would entail a loss of data near the axial extremities of the scanner because a cylindrical geometry could never perfectly fit the four planar detector geometry. This interpolation would also add to the reconstruction time and/or introduce errors. It is unknown if the errors introduced by these interpolations would be significant compared to the approximations used in the PFDR and FORE algorithms. From Theorem IV.4, we see that the PFDR algorithm is more accurate than SSRB in all variables (frequencies), while the Fourier rebinning (FORE) algorithm for sinogram data is less accurate than SSRB for small frequencies. To remedy this inaccuracy, implementation of FORE requires the use of SSRB for small frequencies. This gives an indication that the PFDR algorithm may be more accurate than FORE for small frequencies. The PFDR algorithm has another computational advantage over FORE for the planar imaging geometry other than that resulting from interpolations. Data from different gantry positions can be rebinned independently with the PFDR algorithm. Thus, with the PFDR algorithm, one could rebin the planogram data acquired from one gantry position while data is being acquired at another gantry position. Rebinning with FORE may only be done after full tomographic data is acquired and the data has been interpolated into sinogram coordinates, i.e., only after the scan is complete. If image reconstruction is done with the PFDR algorithm followed by linogram filtered backprojection [10], then each set of data from a different gantry position can be rebinned, filtered (ramp filter), and backprojected independently. With this scheme reconstructions from our PEM-PET system can be reduced by a factor of three if one processor is used and reduced by a factor of six if two processors are used. The computation times presented in Table I do not take this into account.

As stated in the introduction, the motivation for this work was to develop a fast reconstruction algorithm that is suitable for an imaging system capable of detecting lesions of less than 0.5 cm. The PFDR algorithm is certainly fast and computation times are comparable to the SSRB algorithm. As indicated by the reconstructions of the four-quadrant hot sphere phantom (Figs. 4 and 5), the spheres of diameter 0.16 cm and larger are resolved. This resolution is remarkable considering that the detector pixel sampling distance is 0.21 cm. The contrast recovery coefficients of the PFDR algorithm are essentially equal to the reconstructions that use only direct data (which is an exact reconstruction algorithm), while providing superior noise qualities. As indicated in Fig. 6, the noise in the images reconstructed from the SSRB and PFDR algorithms across multiple realizations of the data is similar. This is due to the fact that the noise level is primarily driven by the amount of data used in the reconstruction algorithms which is nearly the equal for the SSRB and PFDR algorithms. However, from Figs. 4 and 5 we see that the noise correlations within an image is significantly greater in the images reconstructed with SSRB as compared with the PFDR algorithm.

The PFDR rebinning algorithm shares many similarities with the work by Kao *et al.* [4]. An in-depth comparison between the PFDR algorithm and Kao's method is beyond the scope of this paper. In Kao's paper, they perform numerical experiments on simulated data with a stack of uniform disks. These images show significant artifacts even in the case of noise-free data. Here we have shown that the PFDR algorithm produces images of high fidelity with both noisey simulated data and data collected from the PEM-PET system. Much of the algorithm analysis presented in Kao's work was done in the (rebinned) data space. Our work is the first to present noise and contrast image metrics for a re-binning method applied to panel detectors.

In this work, we have only considered using the filtered back-projection algorithm to perform our 2-D reconstructions of the rebinned data. As is often done with rebinning

NIH-PA Author Manuscript

NIH-PA Author Manuscript

NIH-PA Author Manuscript

algorithms such as FORE and SSRB, one could use 2-D OSEM to reconstruct each axial slice of the image. If attenuation effects are to be included in the reconstruction, one must reweight the data by the attenuation factors after the rebinning is performed to approximately preserve the Poisson nature of the data, as done in [12].

Acknowledgments

This work was supported by the National Institutes of Health under Grant CA74135 and Grant CA94196.

References

1. Raylman R, Majewski S, Smith M, Kross B, Popov V, Proffitt J, Hammond W, McKisson J, Weisenberger A, Kinahan P, Champley K. Initial testing of a positron emission mammography/tomography (PEM/PET) breast imaging and biopsy device. J Nucl Med. 2007; 48:436.
2. Brasse D, Kinahan PE, Clackdoyle R, Defrise M, Comtat C, Townsend DW. Fast fully 3-D image reconstruction in PET using planograms. IEEE Trans Med Imag. Apr; 2004 23(4):413–425.
3. Edholm PR, Herman GT. Linograms in image reconstruction from projections. IEEE Trans Med Imag. Dec; 1987 MI-6(4):301–307.
4. Kao CM, Pan X, Chen CT. An exact fourier rebinning algorithm for 3-D PET imaging using panel detectors. Phys Med Biol. 2004; 49:2407–2423. [PubMed: 15248586]
5. John F. The ultrahyperbolic equation with 4 independent variables. Duke Math J. 1938:300–322.
6. Defrise M, Liu X. A fast rebinning algorithm for 3-D positron emission tomography using John's equation. Inverse Problems. 1999; 15(4):1047–1065.
7. Johnson CA, Seidel J, Carson RE, Gandler WR, Sofer A, Green MV, Daube-Witherspoon ME. Evaluation of 3-D reconstruction algorithms for a small animal pet camera. IEEE Trans Nucl Sci. Jun; 1997 44(3):1303–1308.
8. Daube-Witherspoon ME, Muehllehner G. Treatment of axial data in 3-D PET. J Nucl Med. 1987; 28:1717–1724. [PubMed: 3499493]
9. Defrise M, Kinahan PE, Clackdoyle R. A note on Fourier rebinning for planograms. 2000 unpublished.
10. Magnusson, M. Linogram and other direct methods for tomographic reconstruction. Dept. Elect. Eng., Linköping Univ; Linköping, Sweden: 1993.
11. Defrise M, Kinahan P, Townsend D, Michel C, Sibomana M, Newport D. Exact and approximate rebinning algorithms for 3-D PET data. IEEE Trans Med Imag. Feb; 1997 16(2):145–158.
12. Comtat C, Kinahan PE, Defrise M, Michel C, Townsend DW. Fast reconstruction of 3-D PET data with accurate statistical modeling. IEEE Trans Nucl Sci. Jun; 1998 45(3):1083–1089.

Appendix

Proof

(Theorem IV.1) Note that $g^{m0} = g$ on $\mathbf{M}_{m0}$. Then for $(u_1, v_1) \in \mathbf{M}_{mH}$

$$\begin{aligned}
\widehat{g}^{m0}_{1100}(U_0, V_0, u_1, v_1) &= \int_{\mathbb{R}} \int_{-v_{m0}}^{v_{m0}} g(u_0, v_0, u_1, v_1) e^{-2\pi i(u_0 U_0 + v_0 V_0)} dv_0\, du_0 \\
&= \int_{\mathbb{R}} \int_{-v_{m0}}^{v_{m0}} \int_{\mathbb{R}} f(u_0 - v_0 y, y, u_1 - v_1 y) \times e^{-2\pi i(u_0 U_0 + v_0 V_0)} dy\, dv_0\, du_0 \\
&= \int_{\mathbb{R}} \int_{-v_{m0}}^{v_{m0}} \int_{\mathbb{R}} f(x, y, u_1 - v_1 y) \times e^{-2\pi i[(x + v_0 y)U_0 + v_0 V_0]} dy\, dv_0\, dx \\
&= \int_{\mathbb{R}} \widehat{f}_{100}(U_0, y, u_1 - v_1 y) \frac{\sin(2\pi v_{m0}(V_0 + U_0 y))}{\pi(V_0 + U_0 y)} dx\, dy \\
&= \widehat{f}_{100}(U_0, y, u_1 - v_1 y) * \frac{\sin(2\pi v_{m0} U_0 y)}{\pi U_0 y}\Big|_{y = -V_0/U_0}.
\end{aligned}$$

Now we have established (3). For (2) we have

$$\widehat{f_{100}}(U_0, y, u_1 - v_1 y) * \frac{\sin(2\pi v_{m0} U_0 y)}{\pi U_0 y}\Big|_{y=-V_0/U_0} = \int_{\mathbb{R}}\int_{\mathbb{R}}\int_{\mathbb{R}} \widehat{f_{111}}(U_0, Y, Z) e^{2\pi i[yY+(u_1-v_1 y)Z]} \times \frac{\sin(2\pi v_{m0}(V_0+U_0 y))}{\pi(V_0+U_0 y)} dy\, dY\, dZ$$
$$= \frac{1}{|U_0|}\int_{\mathbb{R}}\int_{\mathbb{R}} \widehat{f_{111}}(U_0, Y, Z) e^{2\pi i u_1 Z} \times \int_{\mathbb{R}} e^{2\pi i[Y - v_1 Z]y} \frac{\sin(2\pi v_{m0}|U_0|(y+V_0/U_0))}{\pi(y+V_0/U_0)} dy\, dY\, dZ$$
$$= \frac{1}{|U_0|}\int_{\mathbb{R}}\int_{\mathbb{R}} \widehat{f_{111}}(U_0, Y, Z) e^{2\pi i\left[-\frac{V_0}{U_0}Y + \left(u_1 + v_1\frac{V_0}{U_0}\right)Z\right]} \times \mathbf{1}_{\{(U_0,Y,Z):|Y-v_1 Z|\le v_{m0}|U_0|\}}(U_0, Y, Z)\, dY\, dZ.$$

NIH-PA Author Manuscript
NIH-PA Author Manuscript
NIH-PA Author Manuscript

NIH-PA Author Manuscript

NIH-PA Author Manuscript

NIH-PA Author Manuscript

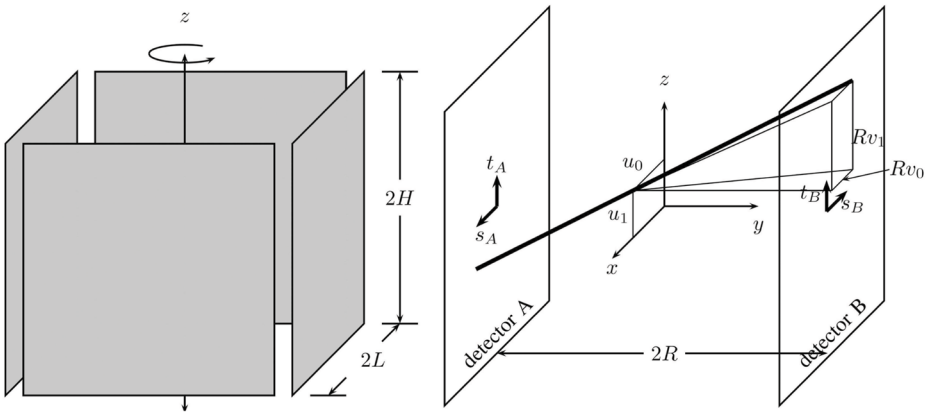

Fig. 1.

Diagram representing the detectors of the PEM-PET system (left). Parameterization of the LORs in the planogram coordinate system (right).

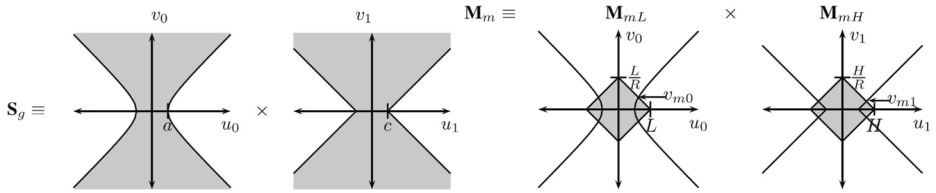

Fig. 2.

The cross product of the two shaded regions represents the support of g, denoted by $\mathbf{S}_g$ (left). The cross product of the two shaded regions represents the measured domain of the planogram transform, denoted by $\mathbf{M}_m$ (right). Here, the boundaries of $\mathbf{S}_g$ have been drawn to illustrate the meaning of the quantities v_{m0} and v_{m1}.

NIH-PA Author Manuscript NIH-PA Author Manuscript NIH-PA Author Manuscript

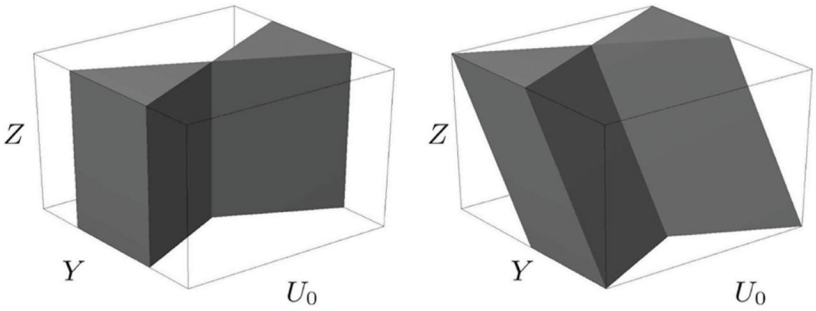

Fig. 3.

Frequency response of the band-pass filter from Theorem IV.1. The filter is supported on the set $\{(U_0, Y, Z): |Y - v_1 Z| \leq v_{m0}|U_0|\}$. Filter shape for direct data, i.e., for $v_1 = 0$ (left). Filter shape for oblique data, i.e., for $v_1 \neq 0$ (right).

NIH-PA Author Manuscript NIH-PA Author Manuscript NIH-PA Author Manuscript

NIH-PA Author Manuscript

NIH-PA Author Manuscript

NIH-PA Author Manuscript

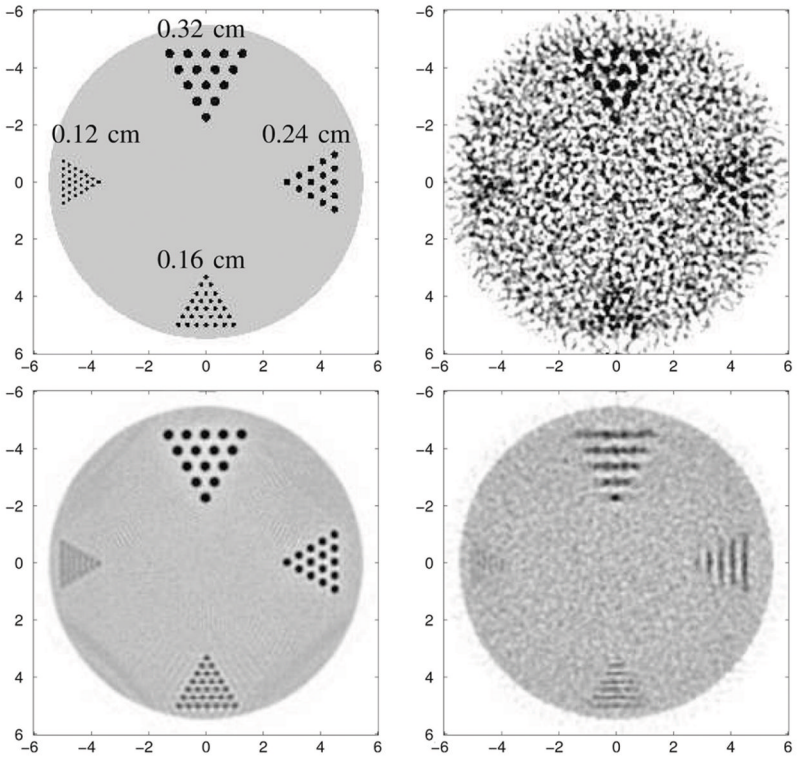

Fig. 4.

Axial slices of reconstructions of noisey four-quadrant hot sphere phantom. Exact phantom (top left). Reconstruction of phantom where we have only used direct data, i.e., the data such that $v_1 = 0$ (top right). Reconstruction from PFDR with $v_{1\max} = \tan(15°)$ (bottom left). Reconstruction from SSRB with $v_{1\max} = \tan(15°)$ (bottom right).

NIH-PA Author Manuscript

NIH-PA Author Manuscript

NIH-PA Author Manuscript

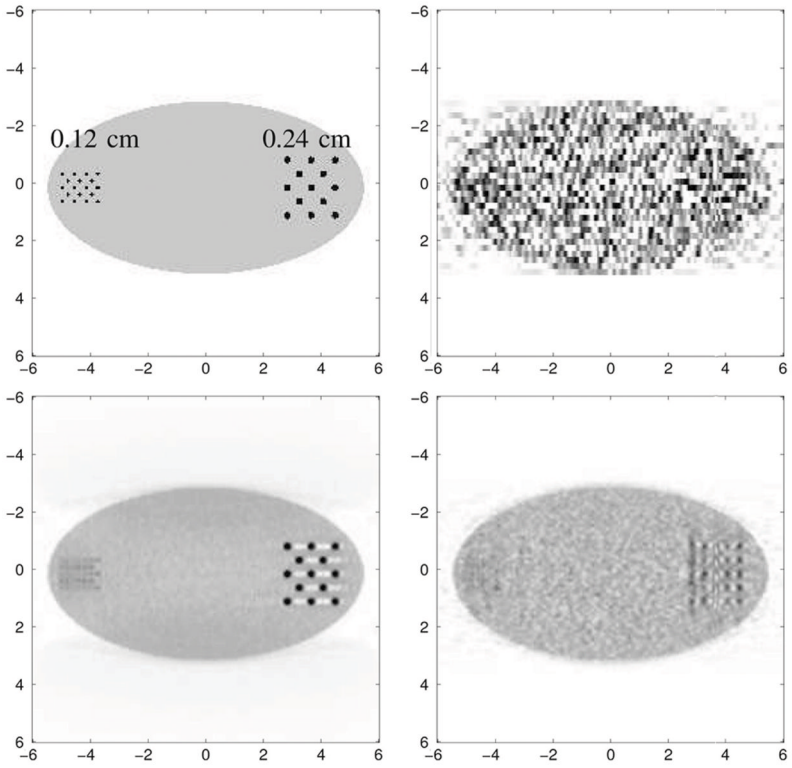

Fig. 5.

Coronal slices of reconstructions of noisey four-quadrant hot sphere phantom. Exact phantom (top left). Reconstruction of phantom where we have only used direct data, i.e., the data such that $v_1 = 0$ (top right). Reconstruction from PFDR with $v_{1\max} = \tan(15°)$ (bottom left). Reconstruction from SSRB with $v_{1\max} = \tan(15°)$ (bottom right).

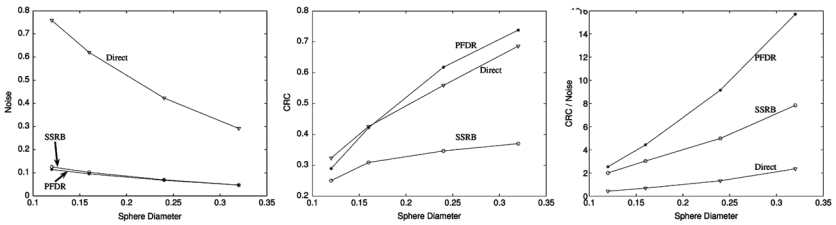

Fig. 6.

Image metrics for four-quadrant hot sphere phantom. Noise in images reconstructed from direct, SSRB, and PFDR algorithms (left). The noise was computed from regions of interest of the background of sizes 0.32, 0.24, 0.16, and 0.12 cm over 20 independent realizations. Contrast recovery coefficients (CRC) for direct, SSRB, and PFDR algorithms for hot spheres (center). Contrast recovery coefficients divided by noise calculations (right).

NIH-PA Author Manuscript NIH-PA Author Manuscript NIH-PA Author Manuscript

NIH-PA Author Manuscript

NIH-PA Author Manuscript

NIH-PA Author Manuscript

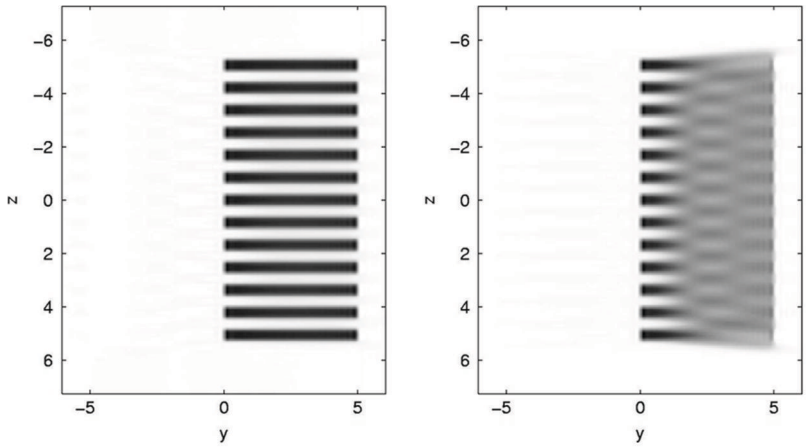

Fig. 7.

Coronal slices of reconstructions of simulated rod source phantom. The rods are of size 5 cm × 0.42 cm × 0.42 cm. Reconstruction using the PFDR algorithm with $v_{1\max} = \tan(15°)$ (left). Reconstruction using the SSRB algorithm with $v_{1\max} = \tan(15°)$ (right).

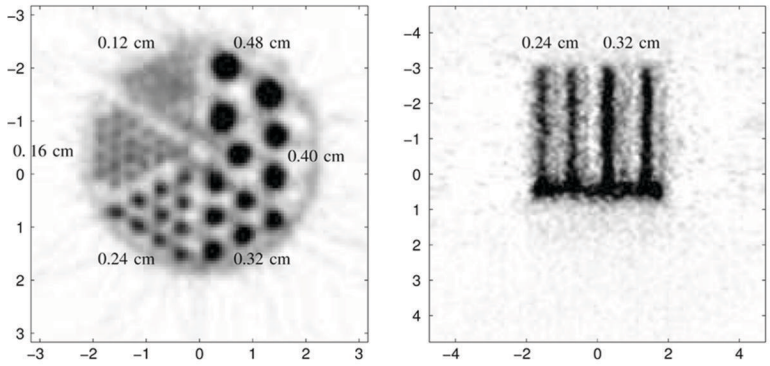

Fig. 8.

Axial and coronal slices of the reconstruction of the micro-Derenzo Phantom from the PEM-PET system. Here, we have used the PFDR algorithm with $v_{1\max} = \tan(15°)$.

NIH-PA Author Manuscript NIH-PA Author Manuscript NIH-PA Author Manuscript

NIH-PA Author Manuscript
NIH-PA Author Manuscript
NIH-PA Author Manuscript

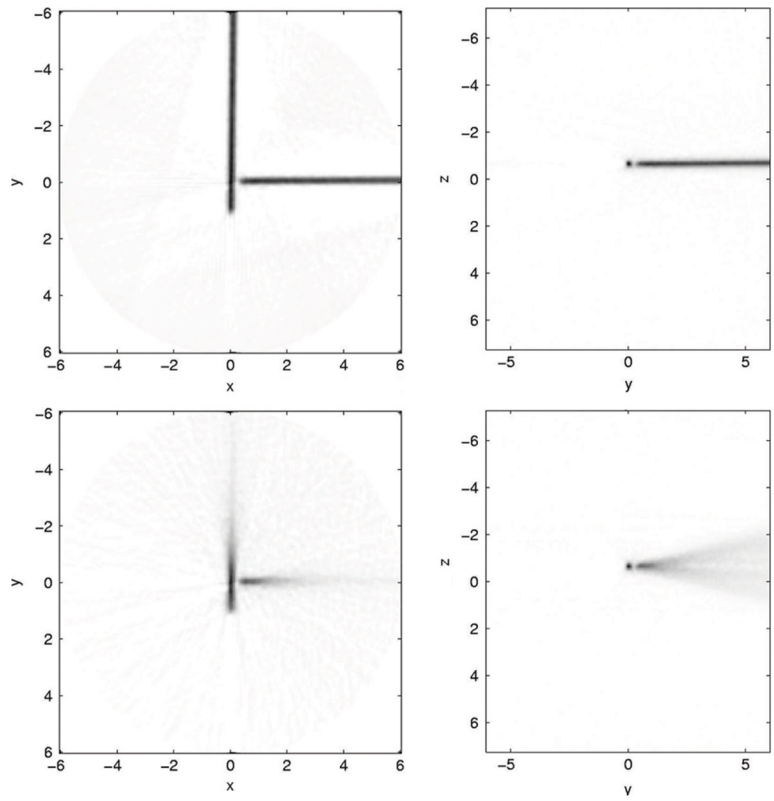

Fig. 9.

Axial and coronal slices of data obtained from the PEM-PET system with a line-source phantom. Axial slice of PFDR reconstruction (top left). Coronal slice of PFDR reconstruction (top right). Axial slice of SSRB reconstruction (bottom left). Coronal slice of SSRB reconstruction (bottom right). For all reconstructions we have used $v_{1\,\max} = \tan(15°)$.

NIH-PA Author Manuscript

NIH-PA Author Manuscript

NIH-PA Author Manuscript

TABLE I

Image Reconstruction Computation Times (sec). Detector Sampling Distance Is Equal to $d = 0.21$ cm

Reconstruction Algorithm	Voxel Side Length d/2 cm	Voxel Side Length d/3 cm	Voxel Side Length d/4 cm
Direct	65	144	376
SSRB	216	407	714
PFDR	251	416	718